Journal of Fluids and Structures 81 (2018) 656–672

Contents lists available at ScienceDirect

Journal of Fluids and Structures

journal homepage: www.elsevier.com/locate/jfs

Numerical study of the wind loads on a cooling tower by a stationary tornado-like vortex through LES

Zhenqing Liu [a,*], Chong Zhang [a], Takeshi Ishihara [b]

[a] School of Civil Engineering and Mechanics, Huazhong University of Science & Technology, Wuhan, Hubei, China
[b] Department of Civil Engineering, School of Engineering, The University of Tokyo, Tokyo, Japan

ARTICLE INFO

Article history:
Received 21 December 2017
Received in revised form 25 May 2018
Accepted 6 June 2018

Keywords:
LES
Cooling tower
Tornado
Numerical analysis
Aerodynamic forces
Spectrum analysis

ABSTRACT

A tornado simulator is built and large eddy simulations are carried out to model the swirling flow fields in a tornado-like vortex and the tornado-induced wind loads on a cooling tower. When the cooling tower is close to the tornado core, the mean and fluctuating loads exerted by the tornado tend to be much larger than those applied by a straight-line wind. However, when the cooling tower is sufficiently far from the center of the tornado, $r > 3.0r_c$, the aerodynamic force coefficients show almost the same value as those induced by the straight-line wind. In the tornado core, the forces show the maximum fluctuations. To explain these large force fluctuations, spectrum analyses are carried out and two peaks are identified. These two peaks are found to be the result of two factors, i.e., the sub-vortices in the tornado and the vortex shedding in the wake of the cooling tower. This is the most important finding in this study, and it clarifies the dynamic response of a cooling tower exposed to a tornado.

1. Introduction

In power plants, the cooling towers are very important structures, which are sensitive to wind forces owing to their significant height and relatively thin wall. The damage to cooling towers caused by straight-line winds has been studied by many researchers. However, only a few studies have focused on tornado-induced damage to cooling towers. Although the reports about tornado-induced damages to cooling towers are limited, serious consequences can arise if a cooling tower cannot resist the tornado-induced forces. In China, many nuclear power plants are being planned, and thus, much more attention should be paid to tornado-induced damages to cooling towers.

Owing to the limited research about tornado-induced wind loads on cooling towers, the features of the aerodynamic forces on other types of structures caused by tornadoes are introduced beforehand in order to provide a general idea about the tornado-induced wind loads. With the aid of tornado-like vortex simulators, i.e., the Ward type (Church et al., 1977, 1979; Diamond and Wilkins, 1984; Mishra et al., 2008; Matsui and Tamura, 2009), ISU type (Haan et al., 2008; Tari et al., 2010; Kikitsu et al., 2011; Cao et al., 2015; Wang et al., 2016, 2017), and WindEEE (Hangan, 2014; Refan and Hangan, 2016), there have been several attempts to physically investigate the wind loads on structures subjected to tornado-like vortices. Jischke and Light (1983) applied a Ward-type simulator to study the tornado induced aerodynamics forces on structures. They proposed that an addition of swirl to the flow provided a significant change in the forces on the model. Mishra et al. (2008) also adopted the Ward-type simulator to generate a tornado-like vortex and examined the forces on a cubical structure. The results show the pressure distribution and have different characteristics compared to those in a straight-line

* Corresponding author.
E-mail address: liuzhenqing@hust.edu.cn (Z. Liu).

https://doi.org/10.1016/j.jfluidstructs.2018.06.001
0889-9746/

Nomenclature

A_i	projected areas of the cooling tower
C_{F_i,V_H}	aerodynamic force coefficients in i (x, y, z) directions
$C_{F_i,V_H,RMS}$	fluctuation of the aerodynamic force coefficients
C_{pe,V_H}	external pressure coefficient
C_s	Smagorinsky constant
d	distance from cell center to the closest wall
D	diameter of the updraft hole
f_i	instantaneous aerodynamic forces
F_i	time averaged aerodynamic forces
H	height of cooling tower
h_{vmax}	height of the globally largest tangential velocity
h_1	height of convergent chamber
l	height of convective chamber
L_s	mixing length for subgrid scales
r	radial distance
P	mean pressure on the ground
P_e	mean pressures acting on external cooling tower surfaces
P_{min}	minimum mean pressure on the ground
P_r	reference pressure
$\tilde{p}$	filtered pressure
Q	flow rate
Re_c	Reynolds number for the cooling tower
Re_t	Reynolds number of the tornado
r_0	radius of updraft hole
r_c	radius at which V_c occurs
r_{Hmax}	radius at which V_{Hmax} occurs
r_L	length ratio
r_s	radius of convergent chamber
r_{vmax}	radial location of the globally largest tangential velocity
r_w	radius of convective chamber
S	swirl ratio
$\tilde{S}_{ij}$	rate-of-strain tensor for the resolved scale
u, v, w	rms of fluctuating streamwise, spanwise, and vertical velocities
$\tilde{u}_i$	filtered velocities
u_τ	friction velocity
U_H	radial velocity at the height of the cooling tower
V_c	maximum tangential velocity in the cyclostrophic balance region
V_H	tangential velocity at the height of the cooling tower
V_{Hmax}	maximum tangential velocity at the height of the cooling tower
w_0	updraft wind velocity at the outlet
x, y, z	Cartesian coordinates

Greek symbols

λ_L	length scale
μ	air viscosity
ω_i	vorticity component of the flow along x_i
Ω	surface of the cooling tower
θ	wind angle at the height of cooling tower
σ	standard deviation of the fluctuating force

wind tunnel. Applying the tornado simulator in Iowa State University, Haan et al. (2009) studied the instantaneous wind load on a gable-roof building with the laboratory-simulated tornado. The results show that the lateral force caused by tornado is 50% higher than that specified by engineering standards (American Society of Civil Engineers 2006, hereafter "ASCE 7-05", Kumar, 2010), and the lift force caused by the tornado is two or three times as large as ASCE 7-05. Rajasekharan et al. (2013a, b) used a tornado simulator at Tokyo Polytechnic University to study the forces caused by a tornado on structures. As in Yang et al. (2010, 2011), significant differences between the forces caused by the tornado and those caused by a straight-line wind

were also identified. A three-dimensional numerical model was used by Alrasheedi and Selvam (2011) to compare the wind load caused by a tornado and the wind load caused by a straight-line wind. They concluded that it is not enough to estimate the wind loads by tornadoes in wind tunnels. Most recently, Liu and Ishihara (2015a) applied three-dimensional large eddy simulations to study the tornado-induced forces on a gable-roof building. In that study, a kind of spiral wind profile was found in the tornado. This spiral is unique compared with profiles in traditional straight-line wind tunnels. However, studies about tornado-induced forces on cooling towers are very scarce and, to the best of the authors' knowledge, only three experimental studies have been conducted.

Cao et al. (2015) and Wang et al. (2016) applied an ISU type tornado simulator in Tongji University to study a stationary tornado and translating tornado-induced wind loads on a cooling tower. They found that the wind pressure caused by a tornado is quite different from that by the traditional straight-line wind. The pressure distribution on the cooling tower exposed to a tornado is found to be asymmetrical and the largest pressure drop on the cooling tower is larger than that induced by the straight-line wind. However, no research has considered the spectrum of aerodynamic forces caused by tornadoes, which is very important for the determination of the dynamic response of a cooling tower.

In this study, a cooling tower exposed to a tornado is simulated. Large eddy simulations are carried out, including the external pressure distribution, aerodynamic forces, and spectrum of the forces. The mechanism of the large fluctuating aerodynamic forces is described. In Section 2, the governing equations, turbulence models, mesh systems, and geometries of the models are introduced. The numerical model is validated in Section 3. Wind loads induced by the tornado-like vortex are discussed in Section 4, including the spectrum properties of the aerodynamic forces in which an important finding will be presented.

2. Numerical models

In this section, the control equations and the solution scheme are introduced first, and then the cooling tower model is presented. The settings of the numerical tornado simulator and numerical wind tunnel are also introduced, including the geometry, grid system, and boundary conditions.

2.1. Governing equations and solution schemes

In the present study, a large eddy simulation (LES) is used, in which large eddies are calculated directly, and the influences of subgrid turbulence are modeled. The Boussinesq hypothesis is adopted and the Smagorinsky–Lilly (Smagorinsky, 1963; Lilly, 1992) model is used to calculate the subgrid-scale (SGS) stresses.

The controlling equations applied in the LES model are obtained by filtering the time-dependent Navier–Stokes equations in Cartesian coordinates (x, y, z):

$$\frac{\partial \rho \widetilde{u}_i}{\partial x_i} = 0 \tag{1}$$

$$\frac{\partial \rho \widetilde{u}_i}{\partial t} + \frac{\partial \rho \widetilde{u}_i \widetilde{u}_j}{\partial x_j} = \frac{\partial}{\partial x_j}\left(\mu \frac{\partial \widetilde{u}_i}{\partial x_j}\right) - \frac{\partial \widetilde{p}}{\partial x_i} - \frac{\partial \tau_{ij}}{\partial x_j} \tag{2}$$

where $\widetilde{p}$ and $\widetilde{u}_i$ are the filtered pressure and velocities, respectively, ρ is the density, μ is the viscosity, and τ_{ij} is the SGS stress, which is determined as follows:

$$\tau_{ij} = -2\mu_t \widetilde{S}_{ij} + \frac{1}{3}\tau_{kk}\delta_{ij}, \qquad \widetilde{S}_{ij} = \frac{1}{2}\left(\frac{\partial \widetilde{u}_i}{\partial x_j} + \frac{\partial \widetilde{u}_j}{\partial x_i}\right) \tag{3}$$

where $\widetilde{S}_{ij}$ is the rate-of-strain tensor for the resolved scale, μ_t is the SGS turbulent viscosity, and δ_{ij} is the Kronecker delta. The Smagorinsky–Lilly model is applied for the calculation of SGS turbulent viscosity:

$$\mu_t = \rho L_s^2 \left|\widetilde{S}\right| = \rho L_s^2 \sqrt{2\widetilde{S}_{ij}\widetilde{S}_{ij}};\ L_s = \min(\kappa d, C_s^{1/2} V^{1/3}) \tag{4}$$

in which L_s is the mixing length for the subgrid scales, κ denotes the von Kármán constant, i.e., 0.42, V is the volume of a computational cell, and d represents the distance to the closest wall. In this study, the Smagorinsky constant C_s is determined to be 0.032 based on Liu and Ishihara (2015a) and Oka and Ishihara (2009).

For the wall-adjacent cells, when they are in the laminar sublayer, the wall shear stresses are obtained from the laminar stress–strain relationship:

$$\frac{\widetilde{u}}{u_\tau} = \frac{\rho u_\tau n}{\mu} \tag{5}$$

If the laminar sublayer cannot be resolved by the mesh, it is assumed that the centroid of the wall-adjacent cells falls in the logarithmic region, and the law-of-the-wall is adopted, expressed as:

$$\frac{\widetilde{u}}{u_\tau} = \frac{1}{\kappa}\ln E\left(\frac{\rho u_\tau n}{\mu}\right) \tag{6}$$

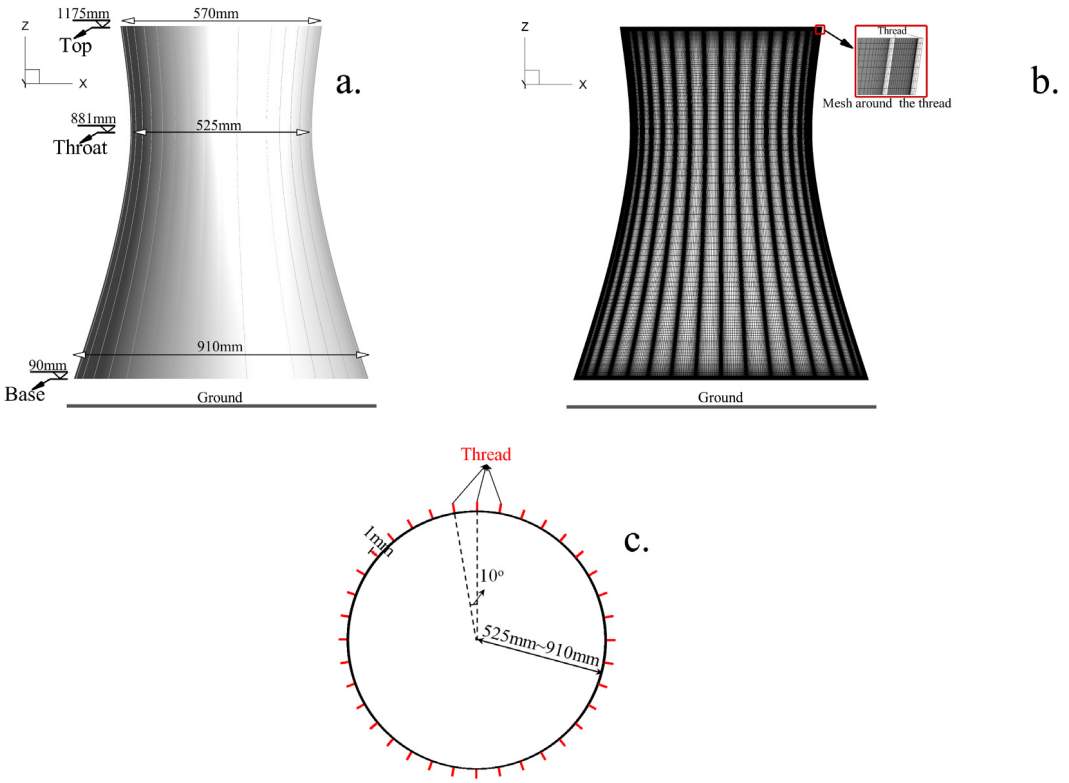

Fig. 1. Configurations of the cooling tower (a), the mesh distribution on the tower surface (b), and (c) the sketch map of the cross section of the cooling tower. The details of the mesh close the threads are shown at the top right corner of Fig. 1(b).

where $\widetilde{u}$ is the filtered velocity tangential to the wall, n is the distance between the center of the cell and the wall, u_τ is the friction velocity, and the constant E is 9.793. If the dimensionless distance from the wall, $n^+ = \rho u_\tau n/\mu$, is larger than 10, Eq. (6) will be applied to close the N–S equation. If n^+ is less than 10, Eq. (5) will be adopted. In the present study, the heights of the grids attaching to the wall are small enough and the resulted n^+ for all of the cases is less than 2.0; therefore only Eq. (5) is applied to close the N–S equations for the grids attaching to the wall.

2.2. Cooling tower model

A cooling tower model, as shown in Fig. 1(a), is chosen, whose height, H, is 235 m, radius of the throat part 105 m, largest radius 182 m, and radius at the top 114 m. The height of the throat is 176.2 m. The height of the gap between the bottom of the cooling tower and the ground is 18 m. The model with a length scale, λ_L, of 1:200 has been studied by Dong et al. (2013) in a straight-line wind tunnel, in which different roughness conditions on the external surface of the cooling tower were studied. In wind tunnel experiments, threads made of very thin paper or aluminum foil are widely used to model the ridge-like structure of the surface of real cooling towers. In the present study, we build the geometry of the threads within the model and apply the wall boundary condition to simulate the roughness of the tower surface. Dong et al. (2013) found that when the external surface is covered by threads with height of 1 mm and width of 0.5 mm every 10°, the wind loads will be not sensitive to the Reynolds number if the upcoming flow is uniform. Considering that in a tornado-like vortex the wind speed is not constant, it is reasonable to choose this surface condition to conduct comparisons between the tornado-induced and straight-line wind loads. In some numerical simulations, the effects of the threads are simply modeled by the roughness height condition using the averaged effects from the thread. In the present numerical simulation, the threads are physically modeled which means the geometry of the threads are directly generated. The numerical cooling tower models applied in the tornado and straight-line wind simulations have the same length scale as those by Dong et al. (2013). Fig. 1(b) shows the mesh system in the present simulations. A blocked structural mesh system is adopted. The vertical mesh varies hyperbolically from 1 mm at the top and base of the tower to 10 mm at the throat. Along the height of the threads, 10 grid cells subdivide the length of each thread and 25 grid cells (ranging in lateral spacing from 1.8 mm at the throat of the tower to 3.2 mm at the base of the tower) subdivide the space between neighboring threads. The height of the grid cells normal to the tower surface is uniformly set to 0.1 mm. The spacing values of the grid attaching the surface of the tower in the direction of flow (h^+), across flow (v^+) and normal to the wall (n^+) in the law-of-wall variables have the maximum of $h^+_{max} = 15$, $v^+_{max} = 67$,

Table 1
Geometry information of the modeling cooling tower.

Height of tower H	Height of the throat	Height of the base clearance	Radius at the throat	Radius at the top	Radius at the base	Thread height	Neighboring threads spacing	Length scale λ_L
1175 mm	881 mm	90 mm	525 mm	570 mm	910 mm	1 mm	10°	1:200

Table 2
Parameters of the wind tunnel simulation.

Height of wind tunnel	Width of wind tunnel	Length of wind tunnel	Location of the cooling tower	Inflow velocity	Cooling tower Reynolds number Re_c	Length scale λ_L
2 m	15 m	14 m	Center of wind tunnel	Uniformly 6 m s^{-1}	0.47×10^6	1:200

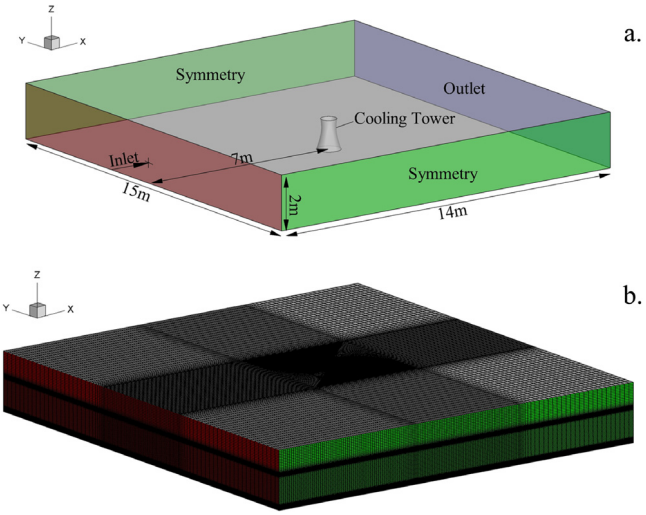

Fig. 2. Configurations of the numerical wind tunnel (a) and the mesh system(b). (For interpretation of the references to color in this figure legend, the reader is referred to the web version of this article.)

and $n^+_{max} = 2$, respectively. In the coarse region, the horizontal grid spacing is 60 mm, and the vertical grid spacing is same in the whole computational domain. The grid used for the background in the center region with a width of 3 m and length of 3 m has horizontal sizes of 7 mm in both x and y directions. The difference between the spacing at the surface of the tower to the background spacing is adjusted linearly with a growing ratio of 1.1. The top right corner of Fig. 1(b) shows the details of the geometry and the grid cells close to the threads. Table 1 summarizes the geometry information of the modeled cooling tower.

2.3. Numerical wind tunnel

A numerical wind tunnel is built as shown in Fig. 2(a), with height of 2 m, width of 15 m, and length of 14 m, which are identical to those in the experiments by Dong et al. (2013). In Fig. 2(a), the orientation is also shown, and x is set as the streamwise direction, y is the crosswind direction, and z is the vertical direction. The cooling tower is located 7 m downstream of the inlet and 7.5 m away from the sides. The velocity at the inlet is uniformly 6 m s^{-1}, and the outflow boundary condition, i.e., the gradients of the flow parameters are zero, is applied at the outlet. The sides (colored by green) and the top of the wind tunnel are set as a symmetry boundary condition. A non-slip boundary condition is applied at the bottom of the wind tunnel and the surfaces of the cooling tower. A blocked structural mesh is used with a coarse mesh near the inlet and a fine mesh in the vicinity surrounding the cooling tower, as shown in Fig. 2(b). The minimum grid size is 0.1 mm in both vertical and horizontal directions. The growing ratios in the two directions and that normal to the surface of the cooling tower are less than 1.1 in order to avoid a sudden change of grid size. The total mesh number is about 9.1×10^6. The Reynolds number for the cooling tower, $Re_c = V_H H/\nu$, is calculated as 0.47×10^6. The parameters used for the wind tunnel simulation are presented in Table 2.

2.4. Numerical tornado simulator

The tornado simulator adopted in the present study is a Ward type, improved by Matsui and Tamura (2009), which could be divided into three parts, i.e., convergence chamber, convection chamber, and exhaust chamber. In the present numerical simulation, the convergent flow was promoted by the velocity profile at the inlet, as shown by red color region in Fig. 3(a). At the top of the exhaust chamber outflow, a boundary condition is applied, as shown by the blue color region in Fig. 3(a). The honeycomb in the experiment is modeled by a porous media in the present numerical simulation, in which there is no drag force in the vertical momentum equation but in the horizontal directions almost infinite drag forces are added. As a result, the fluid in the modeled honeycomb can move freely in the vertical direction but there is nearly no motion in the horizontal directions. These fluid motions in the honeycomb are the same as those applied in the experiments. The numerical methods for modeling the swirling of the flow and the honeycomb have been adopted by Liu and Ishihara (2015b) and showed good performance for reproducing various types of tornadoes. The difference between the present numerical simulator and that by Liu and Ishihara (2015b) is just the geometry size. The length scale, λ_L, is determined by comparing the flow fields with those in the Spencer F4 tornado occurred in Spencer, South Dakota, USA, in 1998, and observed by Wurman and Alexander (2005). The method determining λ_L will be introduced in detail in the following discussion. The selection of $\lambda_L = 1{:}200$ takes into consideration that in the experiment by Dong et al. (2013) λ_L is also 1:200. Therefore, the influence of the Reynolds number for the comparison between the wind loads in the wind tunnel and those in the tornado simulator could be eliminated. The height of the convergent chamber in the present simulation, h_1, is 2 m and the radius of the convergent chamber is $r_s = 10$ m. An updraft hole with radius of $r_0 = 1.5$ m was connected by a convective chamber with height of $l = 6$ m and radius of $r_w = 6$ m. The arrows in Fig. 3(a) indicate the flow rotation direction imposed by the inlet profile, which is anti-clockwise. The tower was tested in a stationary tornado at the locations $(x = 0, y = 0r_c)$, $(x = 0, y = -0.5r_c)$, $(x = 0, y = -1.0r_c)$, $(x = 0, y = -1.5r_c)$, $(x = 0, y = -2.0r_c)$, $(x = 0, y = -2.5r_c)$, $(x = 0, y = -3.0r_c)$, and $(x = 0, y = -3.5r_c)$, which are illustrated by solid black points in Fig. 3(a) and Fig. 4(a), where r_c is the radius at which the maximum tangential velocity, V_c, in the cyclostrophic balance region occurs. Owing to the factor that the height of the tower, H, is just at the cyclostrophic balance region, V_c and r_c are the same as the maximum tangential velocity at the height of the cooling tower, V_{Hmax}, and the corresponding r_{Hmax}, respectively. In the following discussion, it should be kept in mind that $V_c = V_{Hmax}$ and $r_c = r_{Hmax}$, and the symbols V_{Hmax} and r_{Hmax} will not be used from here on. The cooling tower is located on the minus y axis, in part to make the aerodynamic force in the x direction always positive, as in the straight-line wind tunnel. In the following discussion, the radial distance $r = (x^2 + y^2)^{1/2}$ will be adopted.

For the boundary conditions of the numerical tornado simulator, at the inlet, a wind profile formulated as

$$\begin{cases} u_{r_s} = u_1 (z/z_1)^{1/n} \\ v_{r_s} = -u_{r_s} \tan(\phi) \end{cases} \tag{7}$$

is adopted, where u_{r_s} and v_{r_s} are the radial and tangential velocities at $r = r_s$, n equals to 7.0, the reference velocity u_1 and reference height z_1 are set to 0.24 m/s^{-1} and 0.1 m, respectively, and ϕ is the inflow angle, specified as 84.4°. The pressure at the inlet is set as 0. At the outlet, the normal gradients of the velocities and pressure are set as 0. A non-slip boundary condition is applied at the surface of the cooling tower and the bottom and surrounding walls of the simulator, except at the top of the convergence chamber, where a free slip boundary condition is adopted, which is the same treatment as that at the top of the wind tunnel.

Fig. 3(b) shows the mesh system of the numerical tornado simulator. To accurately capture the flow fields of tornado-like vortices and quantitatively investigate the wind loads on the cooling tower, in the central part of the convergent zone and in the vicinity of the ground a fine mesh is considered. The minimum grid size in both the vertical and horizontal directions and the grid growth ratio near the cooling tower are the same as those used in the straight-line wind tunnel, with an attempt to remove the influence from grid differences. The total mesh number is about 9.6×10^6.

The relative locations of the cooling tower and the simulated tornado are illustrated in Fig. 4(a), where the x and y axis are normalized by r_c. Superimposed on Fig. 4(a) is the contour of the normalized mean tangential velocity at H, V_H, by V_c. The thin line with arrows shows the rotation direction of the tornado and the solid blue line indicates the circle at which V_c occurs. Point 1(0°), Point 2(90°), Point 3(180°), and Point 4(270°) are the four external monitoring points at the throat of the cooling tower where the instantaneous pressure will be recorded to examine the dynamic properties of the tornado-induced wind loads, as shown in Fig. 4(a) and Fig. 4(b). The dashed circles with heights of $0.25H$, $0.5H$, and $0.75H$ are the locations at which the pressure distributions will be extracted in both the straight-line wind tunnel and tornado simulations. For the convenience of discussion, the cooling tower surface covered by the brown arc and that by the blue arc in Fig. 4(b) are named as near core region and far core region, respectively.

The Reynolds number for the cooling tower, $Re_c = V_H(r)H/\nu$, is different at each location, and the corresponding values are provided in Table 4. The Reynolds number of the tornado, $Re_t = w_0 D/\nu$, is calculated as 1.6×10^6, where w_0 is the updraft wind velocity at the outlet, 9.55 m s^{-1}, and D is the diameter of the updraft hole. The swirl ratio is defined as proposed by Haan et al. (2008)

$$S \equiv \frac{\pi r_c^2 V_c}{Q} \tag{8}$$

where Q is the flow rate. The parameters r_c, V_c, and Q are measured as 1.2 m, 17.8 m s^{-1}, and 30 m^3 s^{-1}, respectively, therefore the swirl ratio is 2.68. Table 3 lists the important flow parameters in the tornado modeling. Table 4 summarizes

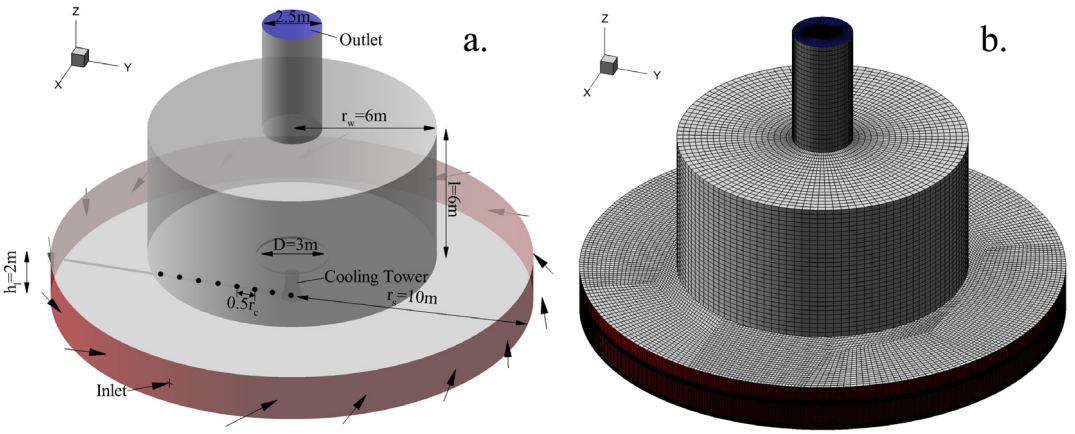

Fig. 3. Configurations of the numerical tornado simulator (a) and the mesh system (b). (For interpretation of the references to color in this figure legend, the reader is referred to the web version of this article.)

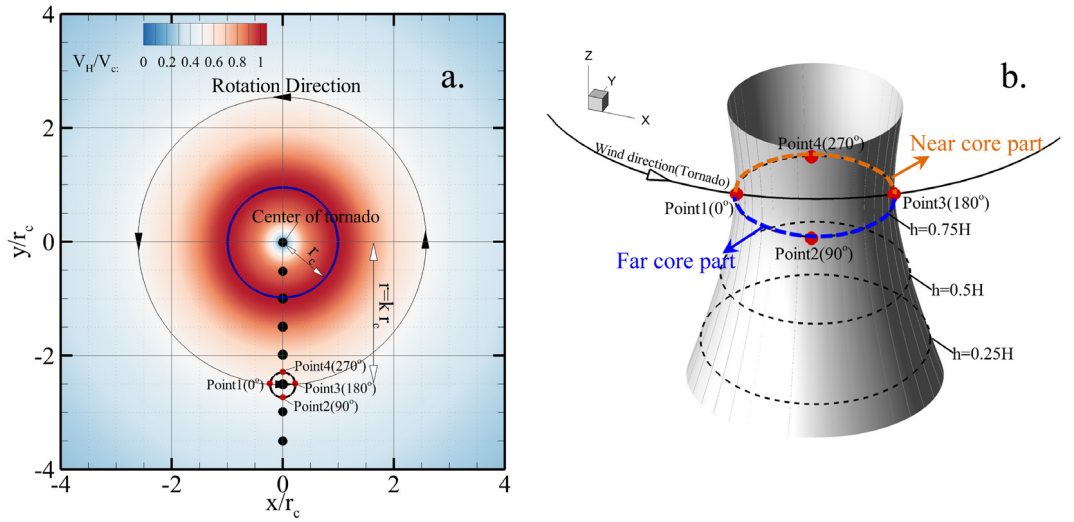

Fig. 4. Relative locations of the cooling tower in the tornado (a) and the monitoring points on the external surface (b). The dashed lines shows the locations at which the mean pressure profile will be plotted.

Table 3
Parameters in the tornado simulation.

Maximum tangential velocity at H	Radius at which V_c occurs	Inflow angle at the inlet	Tornado Reynolds number	Swirl ratio	Ground minimum mean pressure	Flow rate	Updraft wind velocity at outlet	Length scale
V_c	r_c	ϕ	Re_t	S	P_{min}	Q	w_0	λ_L
20.4 m s^{-1}	1.15 m	84.4°	1.6×10^6	2.68	365 Pa	30 m^3 s^{-1}	9.55 m s^{-1}	1:200

the case settings, where P, P_{min}, and θ are the measured mean pressure on the ground at $r = kr_c$, minimum mean pressure on the ground, and wind angle at the height of the cooling tower calculated as $\arctan(U_H/V_H)$ in the tornado-like vortex flow fields, respectively. U_H is the mean radial velocity, with the positive value pointing to the center of the tornado.

2.5. Solution scheme and solution procedure

The simulation uses the finite volume method (FVM), in which the variables were distributed in a non-staggered, cell-centered mesh system. The second-order central difference scheme was used for the convective and viscous terms, and the

Table 4
Case settings for the tornado simulation.

Cases	Radial location	Mean tangential velocity at H with radial distance $r = kr_c$	Mean ground pressure at $r = kr_c$	Angle of attack at H with radial distance $r = kr_c$	Cooling tower Reynolds number at radial distance $r = kr_c$	With cooling tower mounted
	r/r_c	V_H/V_c	P/P_{min}	$\theta_H(^\circ)$	Re_c	Yes/No
Case 0	/	/	/	/	/	No
Case 1	0.0	0.00	1.00	0	/	Yes
Case 2	0.5	0.55	0.81	−1.7	0.86×10^6	Yes
Case 3	1.0	1.00	0.66	0.0	1.56×10^6	Yes
Case 4	1.5	0.92	0.42	1.0	1.43×10^6	Yes
Case 5	2.0	0.72	0.23	1.1	1.12×10^6	Yes
Case 6	2.5	0.61	0.13	1.1	0.95×10^6	Yes
Case 7	3.0	0.53	0.09	1.2	0.83×10^6	Yes
Case 8	3.5	0.45	0.06	1.2	0.70×10^6	Yes

second-order implicit scheme was employed for the unsteady term:

$$\left(\frac{d\phi}{dt}\right)_n = \frac{3\phi^n - 4\phi^{n-1} + \phi^{n-2}}{2\Delta t_n},\ \Delta t_n = t - t_{n-1} = t_{n-1} - t_{n-2} \tag{9}$$

where the indices "n" and "$n-1$" denote the new and old time instances, respectively. The size of the time step Δt was 0.0001 s, and in convective time units it was $\Delta t^* = \Delta t W_0/r = 0.001$. The solution method consisted of linearizing the non-linear equations and implementing a matrix solution. The predicted conjugate gradient (PCG) method was applied to solve the linearized equations along with the algebraic multi-grid (AMG) approach. The Courant–Friedrichs–Lewy (CFL) number was based on the time step size (Δt), velocity (u_i), and grid size (Δx_i), and was expressed as $C = \Delta t\ \Sigma u_i/\Delta x_i$. Here, the CFL number was limited to not exceed 2, $C_{max} = 2$, in the entire computational domain. The semi-implicit pressure linked equations (SIMPLE) algorithm was used to solve the discretized equations. Details for these methods are found in Ferziger and Peric (2002). Relaxation factors were employed to promote the stability of the process. These relaxation factors were 0.3 and 0.7 for pressure and momentum, respectively. Commercial software Ansys Fluent 14.5(2012) was used for the calculations. The initial transient effects were found to disappear after 30 s; therefore, the data for time sampling begins at 30 s and then the flow fields are averaged temporally from 30 s to 80 s.

2.6. Definitions of pressure and force coefficients

The external pressure coefficient C_{pe,V_H} is defined as

$$C_{P_e,V_H} \equiv \frac{P_e - P_r}{0.5\rho V_H^2} \tag{10}$$

in which P_e is the mean pressure acting on the external cooling tower surfaces and P_r is the reference pressure. In the wind tunnel simulation, the pressure reference point is set at the corner of the inlet and the value is zero, and thus, P_r in the wind tunnel simulation is zero. However, in the tornado simulation, the situation is slightly complicated. Rotz et al. (1974) divided the tornado-induced loads on structures into three parts: (1) loads associated with the tornado-induced pressure drop; (2) loads caused by the direct action of the air flow upon the structure; (3) impact loads caused by tornado-borne missiles. In the present study, the third one is not considered. The first part, tornado-induced pressure drop, could be directly obtained from a tornado simulation without the existence of the cooling tower. To perform a comparison with the wind loads by straight-line winds, the effects from the pressure drop will be removed. Therefore, the local pressure drop on the ground is chosen as the reference pressure in the tornado. However, this pressure drop is not a constant. It changes with radial locations. The pressure drops in a tornado as a function of radial distance are provided in Table 4.

Not only the pressure coefficients but also the aerodynamic forces are examined in the present study. The mean aerodynamic forces are normalized as

$$C_{F_i,V_H} \equiv \frac{F_i}{0.5\rho V_H^2 A_i} \tag{11}$$

where C_{F_i,V_H} corresponds to the aerodynamic force coefficients in i (x, y, z) directions. F_i indicates the time-averaged aerodynamic forces, and A_i denotes the projected areas of the cooling tower. The fluctuations of the aerodynamic forces are normalized as

$$C_{F_i,V_H,RMS} \equiv \frac{\sqrt{\sum_{k=1}^{k=N}(f_{i,k} - F_i)^2}}{0.5\rho V_H^2 A_i} \tag{12}$$

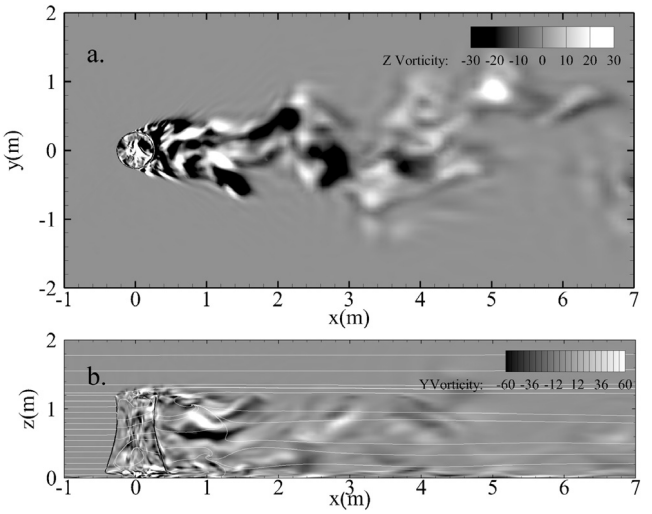

Fig. 5. Vorticity contours on the horizontal slice crossing $z = 0.75$H (a) and that crossing $y = 0$ (b) when the cooling tower is located in the straight-line wind tunnel.

where $C_{F_i,V_H,RMS}$ denotes the fluctuation of the aerodynamic force coefficients and f_i indicates the instantaneous aerodynamic forces, calculated as

$$f_i \equiv \iint_{\Omega} (p - P_r) \cdot n ds \tag{13}$$

in which p is the instantaneous pressure on the surface, Ω, of the cooling tower, and n is the unit vector normal to the infinitesimal surface s.

3. Validation of the numerical models

3.1. Validation of the straight-line wind tunnel

The flow structures around and downstream of the cooling tower exposed to a uniform wind (6 m s^{-1}) are shown by the vorticities in Fig. 5, where Fig. 5(a) depicts the vorticities in z direction, $\omega_z = \partial v/\partial x - \partial u/\partial y$, on the horizontal slice of $z = H$ when $t = 45$ s. The existence of the cooling tower clearly generates a series of vortices. Therefore, in the spectrum analysis of the aerodynamic forces, there should be one peak corresponding to this periodic vortex shedding. As expected, the turbulent structures appear much more detailed around the cooling tower indicating that vortices with very small size have been resolved. The flow close to the structure is not discernibly affected by the outlet or side boundaries, and so it appears that the horizontal domain size is large enough. Fig. 5(b) presents the plotting of the y component vorticities, $\omega_y = \partial w/\partial x - \partial u/\partial z$, on the vertical slice of $y = 0$. The streamlines, plotted by the thin solid white lines, are superimposed and the directions are determined by the mean streamwise and vertical velocities. It can be found that owing to the gap between the tower base and the ground, the flow could penetrate from here to the downstream wake region, disturbing the near boundary layer flow. The height of the computation domain, 2 m, is identical to that in the experiments by Dong et al. (2013), and this height appears to be acceptable because the top does not have a discernible influence on the region of concern as shown in Fig. 5(b). The mean external pressure coefficients at three elevations are shown in Fig. 6. C_{P_e,V_H} is found to show two negative peaks at 60° and 300°, independently of how high the elevation is. The experimental results at $h = 0.75$H by Dong et al. (2013) are also provided for comparison, and they are found to be quite comparable with those in the numerical simulations, except the regions near 180°, where the absolute experimental results are slightly larger than those in the simulations, with discrepancies of approximately 15%. These minor discrepancies may be due to the slight difference in roughness between the cooling tower surface in the numerical simulation and the cooling tower surface in the wind tunnel experiment.

3.2. Validation of the tornado simulator

In the previous presentation, the length scale of the tornado simulator is 1:200. Here the method determining the length scale is introduced briefly. Hangan and Kim (2008) proposed a length ratio, i.e., $r_L = r_{vmax}/h_{vmax,}$ to relate the simulated vortices to the full-scale Spencer tornado, where r_{vmax} is the radial location of the globally largest tangential velocity and h_{vmax} is the corresponding height. $r_L = 6.0$ in the Spencer tornado is found to be almost equal to that, $r_L = 6.1$, in the present

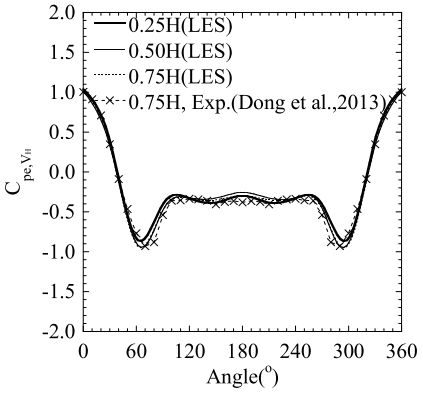

Fig. 6. Mean external pressure coefficient distributions on the cooling tower exposed to the straight-line wind.

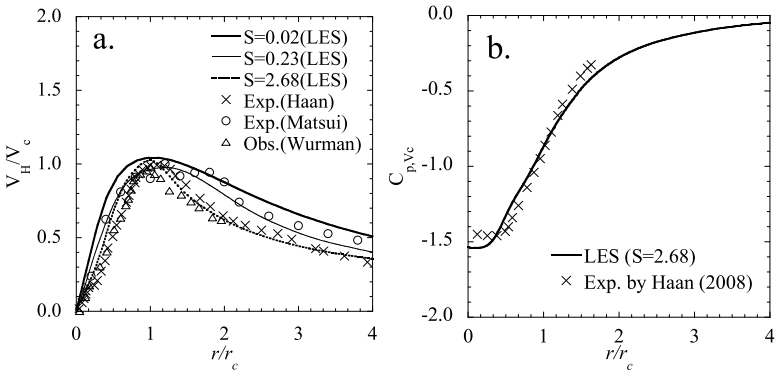

Fig. 7. Radial distribution of the mean tangential velocity at H normalized by V_c at various swirl ratios (a) and radial distribution of the pressure on the ground normalized by V_c (b).

modeled tornado. As a result, the length scale ratio, $r_{vmax,p}/\ r_{vmax,m}$, is 200, where $r_{vmax,p}$ is equal to 120 m and $r_{vmax,m}$ is 0.6 m. Moreover, the velocity scale, $V_{vmax,p}/\ V_{vmax,m}$, is 3.0, where $V_{vmax,p}$ is 81 m s^{-1} and $V_{vmax,m}$ is 27 m s^{-1}. The subscripts "$_p$" and "$_m$" represent the values in the Spencer tornado shown by Kuai et al. (2008) and those in present study, respectively. The length and velocity scales are further investigated by comparing the scaled V_c and r_c in the simulation with those for the Spencer tornado. The values are 61.2 m s^{-1} and 230 m in the present simulations in scale and 65 m s^{-1} and 220 m for the Spencer tornado. Actually, nine simulations with different swirl ratios ($S = 0.01$, 0.02, 0.06, 0.12, 0.23, 0.73, 1.69, 2.68, and 3.12) were carried out without the cooling tower. Furthermore, the case with swirl ratio of 2.68 is found to have the length ratio r_L most close to that of the Spencer tornado. Fig. 7(a) shows comparisons of normalized mean tangential velocity by V_c in the cyclostrophic balance region at $S = 0.02$, 0.23, and 2.68. The best comparison with the observation of the Spencer tornado by Wurman and Alexander (2005) is found to be from the case of $S = 2.68$, further verifying the length scale determined in the present study. The experiment by Matsui and Tamura (2009) reproduced a tornado at the touching down stage, which corresponds to the case of $S = 0.23$ in our simulation, and a good agreement is achieved. The data in the experiment by Haan et al. (2008) is superimposed, which is the reproduction of the Spencer tornado using the simulator in Iowa State University, and good agreement with the case of $S = 2.68$ is also shown, thus validating the numerical method in the present tornado simulation. The mean pressure drop on the ground caused by the rotation of flow in the tornado is depicted in Fig. 7(b) and normalized by V_c, showing a relative flat curve from $r = 0r_c$ to $r = 0.4r_c$, which is also captured in the experimental study by Haan et al. (2008).

4. Wind loads on the cooling tower caused by the tornado

4.1. Patterns of the flow around the cooling tower

The flow patterns around the cooling tower are firstly examined as shown in Fig. 8. In the figure, the vorticity in the z direction at the horizontal slice crossing the throat of the tower is drawn, on which are superimposed the vectors whose length indicates the relative wind speed and the arrows indicate the directions. The x and y components of the vectors are

determined from the mean velocities in the x and y directions. At $r = 0.0r_c$, there is no obvious wake owing to the symmetry of the flow here. Increasing the radial distance to $r = 0.5r_c$, the vortex shedding emerges, and it is obvious that the vortex shedding is not symmetrical. At the far core part, referred to by the blue dashed line in Fig. 4(b), the shedding is stronger than that at the near core part, indicated by the brown dashed line in Fig. 4(b). This may be due to the larger upcoming wind speed at the far core part than that at the near core part. The curvature of the flow may also contribute to the asymmetry of the vortex shedding. Further increasing the radial distance to the boundary of the core, the tangential velocity is the maximum. We can see that the separation and stagnation points could be clearly identified. Moreover, the upcoming flow separates at locations close to those where the tower is exposed to the straight-line wind. With further increase in radial distance, the contrast of the color becomes weak owing to the decrease in the upcoming wind speed. Furthermore, the vortex shedding tends to become symmetrical owing to the decrease in the curvature of the upcoming rotating fluid.

4.2. Mean wind loads

Mean external pressure distributions at various radial locations are plotted in Fig. 9, where the pressure has been normalized by V_H. The heights for the plotting of mean pressure have been illustrated by dashed lines in Fig. 4. At the location of $r = 0.0r_c$, because of the zero tangential velocity, the pressures, with the atmospheric pressure drop removed, are directly plotted without normalization. The resulted pressure distribution here, on the external surface of the tower, does not vary substantially and the values just scatter around 0 Pa. This means that only the tornado, which causes atmospheric pressure drop, contributes to the external pressure here. At $r = 0.5r_c$ the pressure distribution drops at 90 degrees and 300 degrees, indicating flow separation. The drop at the far core part is found to be larger than that at the near core part, which is also observed at the other locations. The largest external pressure drop on the tower occurs at the locations $r = 1.5r_c$, reaching to -2 at the height of 0.75H. The experimental data by Cao et al. (2015) are also plotted in Fig. 9(c) and Fig. 9(d). The data from Cao et al. (2015) is for a case where the cooling tower is located at $r = 1.2r_c$ and the surface of the cooling tower is smooth. The asymmetrical trends of the pressure coefficient profiles are the same, but the values show relatively large discrepancies. These discrepancies may result from the different Reynolds number and different roughness condition of the surface of the cooling tower.

The location of the stagnation point is found to be different to that when the wind is uniformly straight. In the tornado situation, the stagnation point shifts to the near core part, as shown in Fig. 8(e∼h) and Fig. 9(e∼h) in comparison with the experimental data from Dong et al. (2013); however, this shift becomes smaller as the radial distance increases. The discrepancy between the tornado-induced external pressure coefficient and that by the straight-line wind is the least at $r = 3.5r_c$.

The mean aerodynamic force coefficients for the tower exposed to the tornado are compared with those in the straight-line wind tunnel, as shown in Fig. 14. The formulations determining the aerodynamic force coefficients are found in Eq. (11). As has been mentioned, the tangential velocity at the center of the tornado is zero, and thus, it is impossible to provide the force coefficients here. Therefore, only the force coefficients from $r = 0.5r_c$ to $r = 3.5r_c$ are drawn. C_{Fx,V_H} at $r = 0.5r_c$ is much smaller than that in the wind tunnel; however, it increases quickly as the radial distance increases, showing its peak at $r = 1.5r_c$, followed by a decrease to 0.7 at $r = 3.5r_c$, which is nearly equal to the wind tunnel result, as could be found in Fig. 10(a). Owing to the existence of the wind angle, θ, in the upcoming flow in the tornado, as presented in Table 4, there should be a y component force when the cooling tower is exposed to a tornado-like vortex. The force coefficient of the y component is shown in Fig. 10(b), which tends to increase from the inner core region to $r = 1.5r_c$, then decreases, and at last becomes equal to that in the wind tunnel. The most interesting trend is the force coefficient in vertical direction. Different from the force coefficients in the x and y directions, the vertical force coefficient shows its maximum in the inner core region, as seen in Fig. 10(c). However, this large positive vertical force decreases, then turns negative, and becomes approximately -0.4 at $r = 3.5r_c$. The positive vertical force coefficient at the inner core region of the tornado should be due to the large vertical wind velocity near its core boundary. However, this vertical wind becomes weak as the radial distance increases; as a result, it finally shows almost the same value as that of the straight-line wind.

4.3. Fluctuating wind loads

The aerodynamic force fluctuations are measured and shown in Fig. 11. For all of the fluctuation components, we can find that the values show their maximum at the inner core of the tornado; however, they decrease to a value close to that with the straight-line uniform wind, indicating that the upcoming wind condition becomes almost straight-line and laminar in the outer region of tornado. This has been confirmed in the systematic study of the tornado-like vortex by Liu and Ishihara (2015b). The large turbulence in the inner core of the tornado should be the reason for the large force fluctuations here, implying that to apply the results from the wind tunnel to determine the fluctuation of wind loads caused by tornadoes much more attention should be paid to the inner region of the tornado. It is interesting that the vertical aerodynamic force fluctuation gives a quite large value at $r = 0.5r_c$. This large value should be due to the large vertical velocity here and the subsidiaries passing though the cooling tower. In the following discussion about the power spectrum of the aerodynamic forces, the mechanism of the fluctuating aerodynamic forces will be examined.

A spectrum analysis of the aerodynamic forces is important for the dynamic analysis of structures. To our best knowledge, this is the first time that the spectrum of aerodynamic forces for a structure exposed to a tornado-like vortex is obtained.

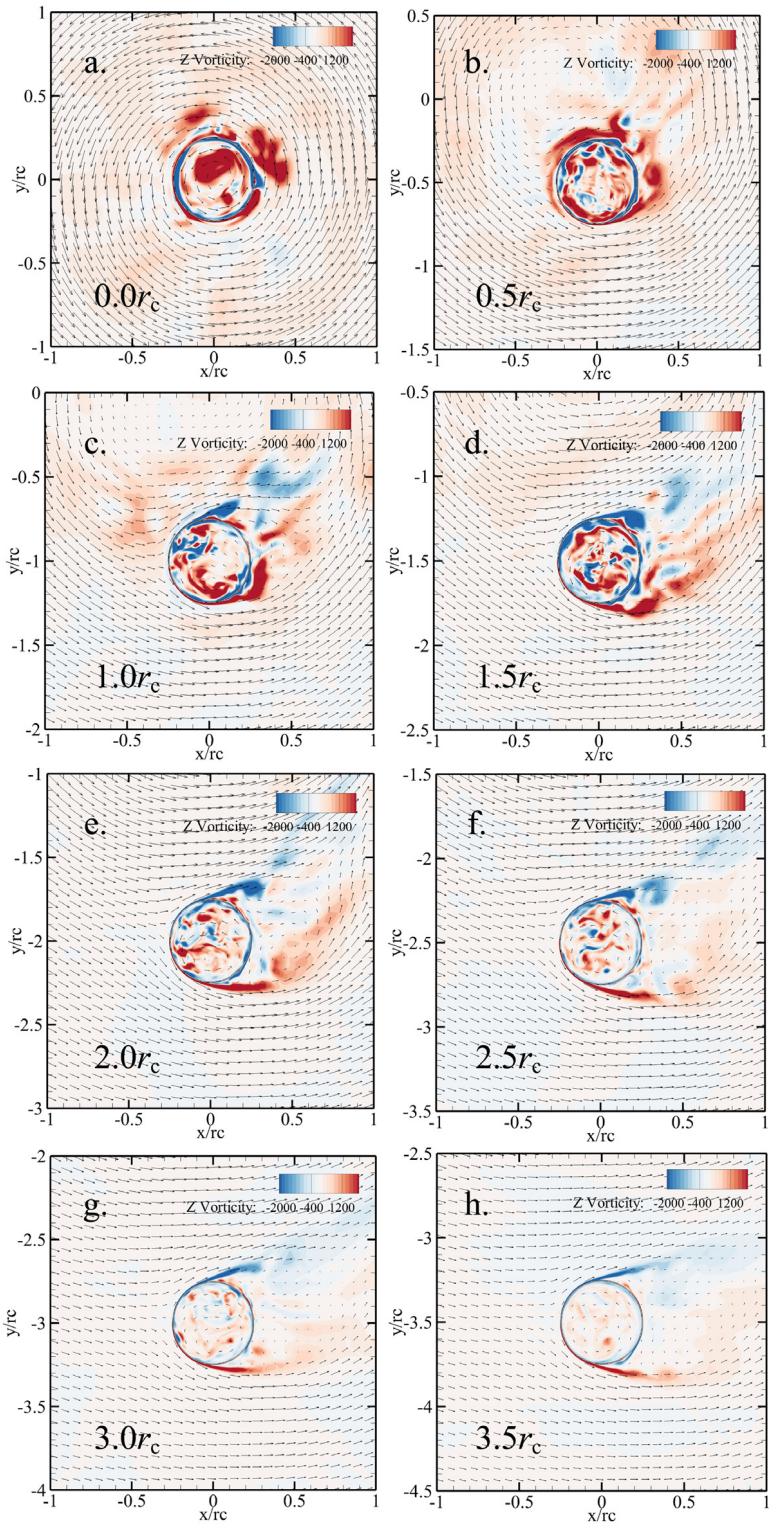

Fig. 8. Distributions of the vertical vorticity at the horizontal slice of $z = 0.75$H when the cooling tower is located at (a) $r = 0.0r_c$, (b) $r = 0.5r_c$, (c) $r = 1.0r_c$, (d) $r = 1.5r_c$, (e) $r = 2.0r_c$, (f) $r = 2.5r_c$, (g) $r = 3.0r_c$, and (f) $r = 3.5r_c$.

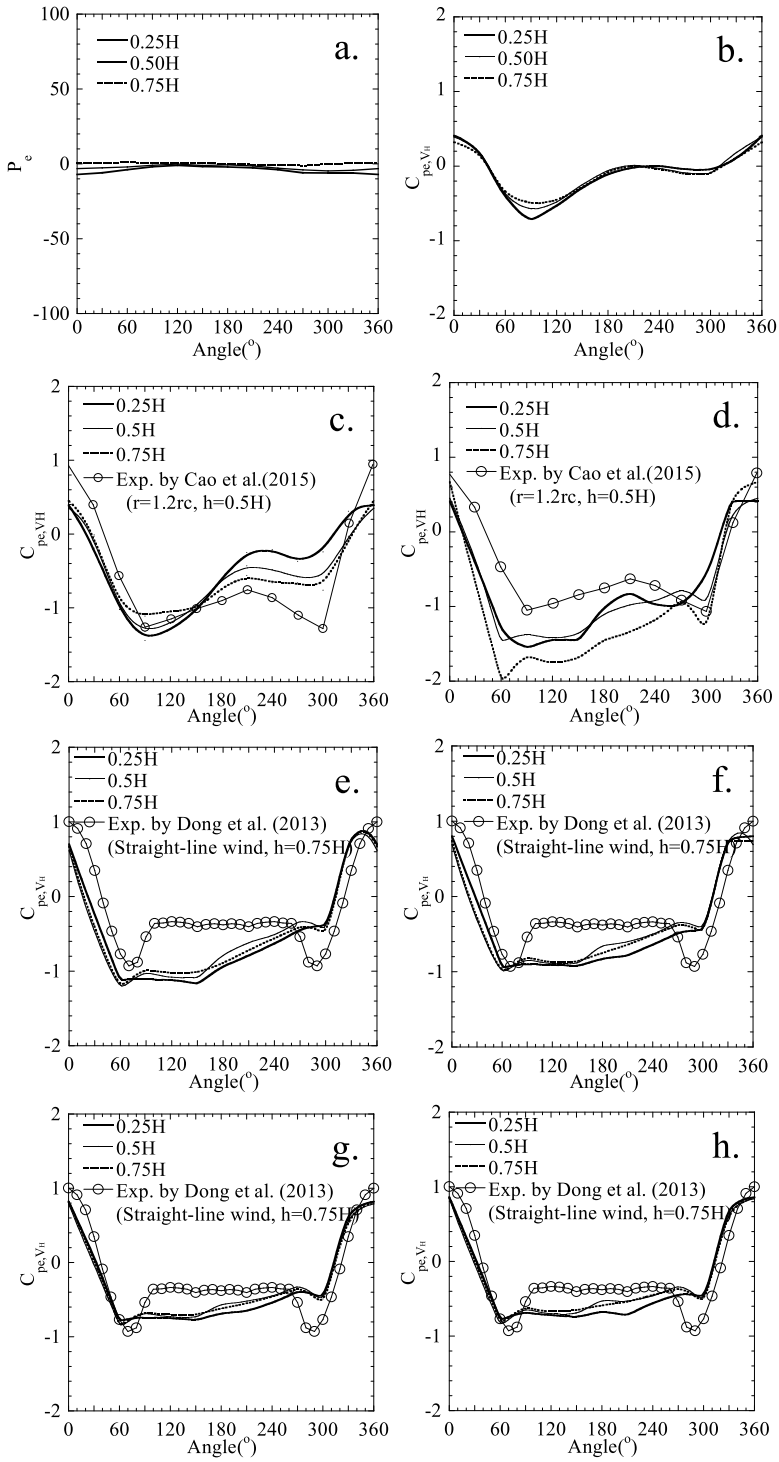

Fig. 9. External pressure coefficients normalized by V_H at height of $0.25H$, $0.50H$ and $0.75H$ when the cooling tower is located at (a) $r = 0.0r_c$, (b) $r = 0.5r_c$, (c) $r = 1.0r_c$, (d) $r = 1.5r_c$, (e) $r = 2.0r_c$, (f) $r = 2.5r_c$, (g) $r = 3.0r_c$, and (f) $r = 3.5r_c$. The locations plotting this figure have been illustrated by dashed lines in Fig. 4.

Among the aerodynamic forces in the three directions, the major component is that in the *x* direction caused mainly by the tangential velocity in the tornado. Therefore, only the power spectrum of forces in the *x* direction will be analyzed, which is calculated by the Maximum Entropy Method (MEM). Maximum entropy spectral estimation is a method of spectral density

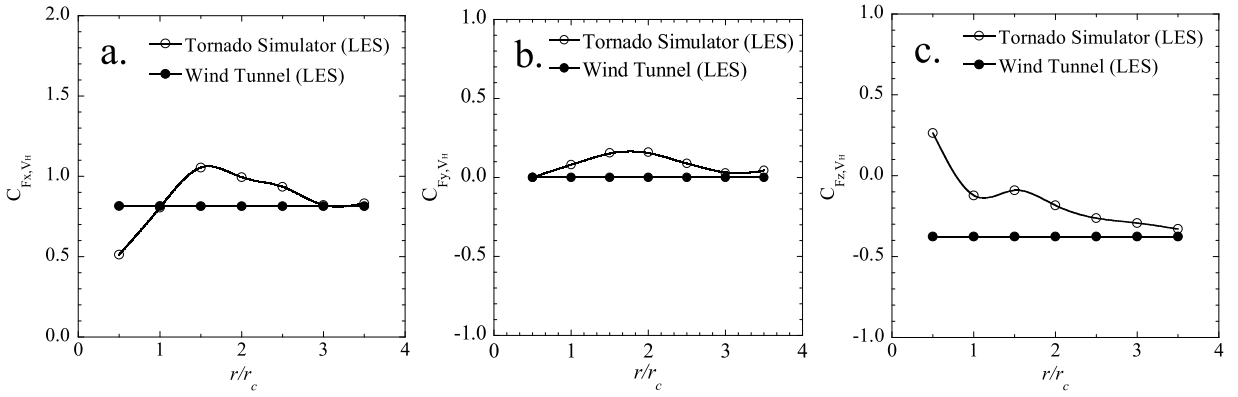

Fig. 10. Aerodynamic force coefficients normalized by V_H as a function of radial distance, (a) x component, (b) y component, and (c) z component.

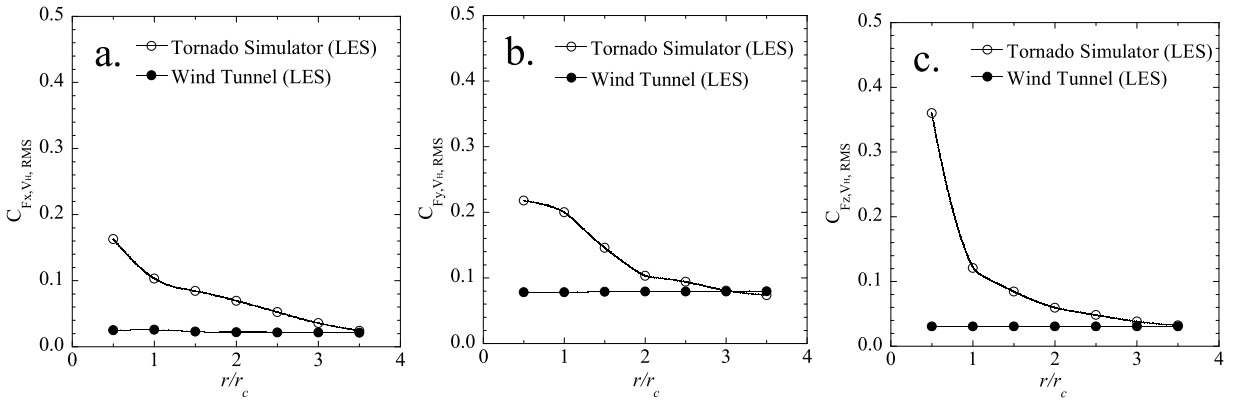

Fig. 11. Root mean square of the fluctuating aerodynamic force normalized by V_H as a function of radial distance, (a) x component, (b) y component, and (c) z component.

estimation. The goal is to improve the spectral quality based on the principle of maximum entropy. The method is based upon an extrapolation of a segment of a known autocorrelation function for lags which are not known. In this way the characteristic smearing of the estimated PSD due to the truncation of the autocorrelation function can be removed. More detailed introduction about this method could be found in the studies by Kay and Marple (1981) and Press et al. (2007).

In Fig. 12(a) the horizontal axis is normalized using V_H/H (it needs to be mentioned $V_H(r = 0.5r_c)/H$ is used for the normalization of the x axis when the cooling tower is located at $r = 0.0r_c$) and the vertical axis is normalized by σ^2/n, where σ is the standard deviation of the fluctuating forces. The resulted spectrum curves for the cases with radial locations equal to $0.0r_c, 0.5r_c, \ldots, 3.5r_c$ and that in wind tunnel are illustrated. From the plotting of the power spectrum of fluctuating aerodynamic forces in the x direction, two peaks could be clearly identified. The smaller one occurs at about $n\,H/V_H = 0.17$ which is also the sole peak when the cooling tower is exposed to the straight-line wind. As seen in Fig. 5(a), we know that this peak is due to the generation of the Karman vortex street. At $r \geq 1.0r_c$ the spectrum curve gives only one peak located at about $n\,H/V_H = 0.17$, implying the similarity of the flow pattern with that in the straight-line wind situation. An interesting aspect could be found for the cases at $r = 0.0r_c$ and $r = 0.5r_c$, where the spectrum shows the peak at the frequency of $2.0 < n2\pi r_c/V_c < 3.0$, where $V_c/2\pi r_c$ corresponds to the tornado core rotation frequency. Therefore, $2.0 < n2\pi r_c/V_c < 3.0$ implies nearly three times the tornado-core rotation frequency that occurs when the tower is located in the core region. In order to clarify this interesting phenomenon, the instantaneous flow fields of the tornado will be examined.

Snapshots of the tornado-like vortex are shown in Fig. 13. The figures are drawn using pressure iso-surfaces with transparency effect to show the subsidiaries in the vortex. Three sub-vortices could be clearly identified, even though their intensity is different. As has been mentioned by Snow (1982), the subsidiary is not stable. It tends to be strong, then dissipate, and finally a new sub-vortex is continuously generated. This periodic character is reproduced in the present study. We focus on one sub-vortex, denoted by the red dashed line. In Fig. 13(a), it can be found that this subsidiary is intense. Advancing the time, this sub-vortex becomes weak, as seen in Fig. 13(b), and then dissipates, as shown in Fig. 8(c). At last, a new subsidiary is generated, as depicted in Fig. 8(d). It has been reported by Monji (1985) that there exists an additional pressure drop in the subsidiary, and therefore, the existence of the subsidiary in the vortex may give a periodic wind load to the structures.

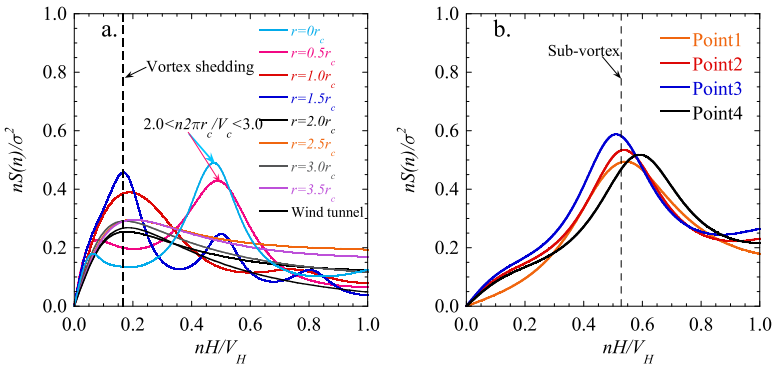

Fig. 12. Power spectrum of the aerodynamic forces in x direction when the cooling tower is mounted at various radial locations (a) and the power spectrum of the pressure at the monitoring points when the cooling tower is located at the center of tornado (b).

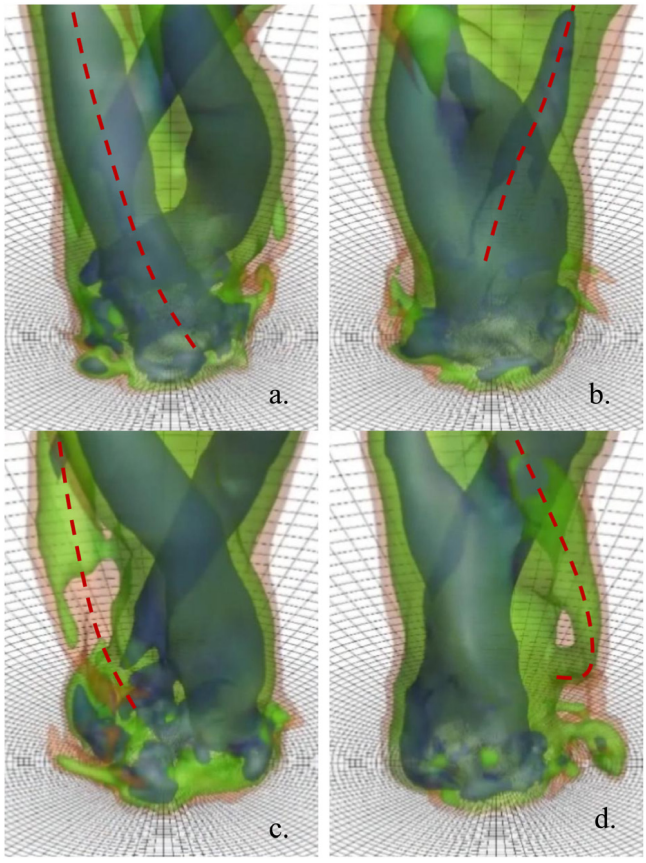

Fig. 13. Instantaneous pressure iso-surfaces at four continuous time points when the cooling tower is not introduced in the tornado simulator, (a) $t = 30.12$ s, (b) $t = 30.21$ s, (c) $t = 30.29$ s, (d) $t = 30.37$ s.

The existence of the subsidiaries should be the reason the nearly three times of the tornado-core rotation frequency for the aerodynamic forces when the cooling tower locates at $r = 0.0r_c$ and $r = 0.5r_c$.

The instantaneous pressures at the four monitoring points, Point1, Point2, Point3, and Point4 are also analyzed when $r = 0.0r_c$, where the peak at $2.0 < n2\pi r_c/V_c < 3.0$ in the spectrum is the most obvious, as shown in Fig. 12(b). It is a further confirmation that the aerodynamic fluctuations are caused mainly by the subsidiaries when the structure is located in the tornado core region. Four continuous snapshots of the instantaneous pressure distribution on the slice crossing the throat of the cooling tower are shown in Fig. 14, where three sub-vortices could be clearly observed and named as sub-vortex1, sub-vortex2, and sub-vortex3, in order. The thick solid line indicates the surface of the cooling tower. It can be found that

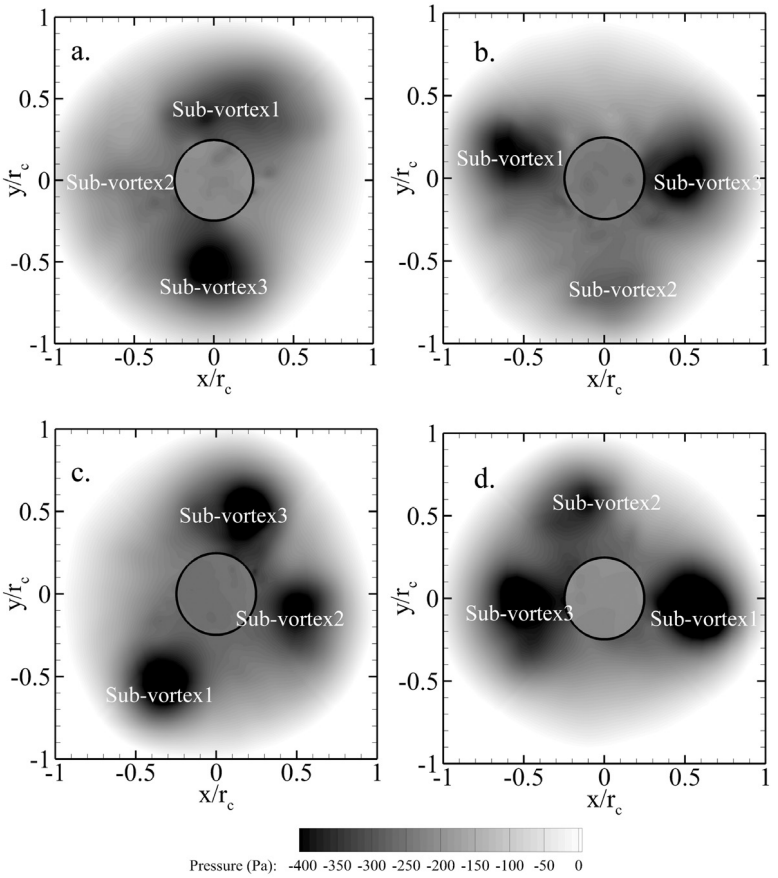

Fig. 14. Snapshots of the instantaneous pressure distribution when the cooling tower is mounted at the center of tornado at (a) $t = 32.15$ s, (b) $t = 32.23$ s, (c) $t = 32.32$ s, and (d) $t = 32.40$ s.

in the three subsidiaries there exists an additional pressure drop. This pressure drop touches on the external surface of the cooling tower providing a periodic change in the external pressure. As a result, a frequency nearly three times as large as that of the tornado core rotation is generated.

5. Conclusions and discussion

In the present numerical study of the wind loads on a cooling tower exposed to a tornado-like vortex, a large eddy simulation is applied. The largest horizontal force coefficient appears at around $r = 1.5r_c$, and the maximum vertical force coefficient appears at the inner core region of the tornado. The fluctuation of the aerodynamic force coefficients increases with decreasing radial distance. When the radial distance is $r = 3.5r_c$, the mean force coefficients and the fluctuating ones become almost the same as those in wind tunnel simulations. Two factors affect the tornado-induced aerodynamic forces, i.e., the sub-vortex and vortex shedding. The effect from the sub-vortex is the most obvious at the inner core of the tornado. When the radial location of the cooling tower is $r \geq 1.0r_c$, the spectrum curve reveals the peak, as in the case of the wind tunnel simulation. This means that vortex shedding is the major contribution of the aerodynamic force fluctuations in the outer region of a tornado.

It should be noted that the inflow in the present simulation is nearly laminar. While this is frequently seen in vortex chamber simulations, it can be problematic as discussed by Bryan et al. (2017). In reality, the inflow should be turbulent as well, and the presence or lack of turbulence in the inflow can substantially affect the structure and intensity of the vortex core (Nolan et al., 2017; Dahl et al., 2017). The Reynolds number in the simulation is not as large as that in nature, but high Reynolds number could affect the flow structure greatly, as has been studied by Rotunno et al. (2016). In the future, the inflow condition as well as the Reynolds number should be examined. While the power spectra in this study provide key insights into sources of structural stress in tornadic circulations, those insights can be clarified by performing and analyzing simulations with turbulent inflow and high Reynolds number as well.

Acknowledgments

The supports from the National Key Research and Development Plan of China (2016YFE0127900, 2016YFC0800200), the National Natural Science Foundations of China (51608220), and the Project of Innovation-driven Plan in Huazhong University of Science and Technology (2017KFYXJJ141), are gratefully acknowledged.

References

Alrasheedi, N.H., Selvam, R.P., 2011. Tornado forces on different building sizes using computer modeling. In: ASME Early Career Technical Conference, United States.
Bryan, G.H., Dahl, N.A., Nolan, D.S., Rotunno, R., 2017. An eddy injection method for large-eddy simulations of tornado-like vortices. Mon. Weather Rev. 145, 1937–1961.
Cao, S., Wang, J., Cao, J., Zhao, L., Chen, X., 2015. Experimental study of wind pressures acting on a cooling tower exposed to stationary tornado-like vortices. J. Wind Eng. Ind. Aerodyn. 145, 75–86.
Church, C.R., Snow, J.T., Agee, E.M., 1977. Tornado vortex simulation at Purdue University. Bull. Am. Meteorol. Soc. 58 (9), 900–908.
Church, C., Snow, J.T., Baker, G.L., Agee, E.M., 1979. Characteristics of tornado-like vortices as a function of swirl ratio: A laboratory investigation. J. Atmos. Sci. 36 (9), 1755–1776.
Dahl, N.A., Nolan, D.S., Bryan, G.H., et al., 2017. Using high-resolution simulations to quantify underestimates of Tornado intensity from in situ observations. Mon. Weather Rev. 145 (5).
Diamond, C.J., Wilkins, E.M., 1984. Translation effects on simulated tornadoes. J. Atmos. Sci. 41 (17), 2574–2580.
Dong, R., Zhao, L., Ge, Y.J., Ke, S.T., 2013. Investigation of surface roughness and its influence to flow dynamic characteristics of hyperbolic cooling tower. Acta Aerodyn. Sin. 31 (2), 250–259.
Ferziger, J., Peric, M., 2002. Computational Method for Fluid Dynamics, third ed. Springer.
Haan, F.L., Balaramudu, V.K., Sarkar, P.P., 2009. Tornado-induced wind loads on a low-rise building. J. Struct. Eng. 136 (1), 106–111.
Haan, F.L., Sarkar, P.P., Gallus, W.A., 2008. Design, construction and performance of a large tornado simulator for wind engineering applications. Eng. Struct. 30 (4), 1146–1159.
Hangan, H., 2014. The wind engineering energy and environment (WindEEE) dome at Western University, Canada. Wind Eng., JAWE 39 (4), 350-35.
Hangan, H., Kim, J.D., 2008. Swirl ratio effects on tornado vortices in relation to the fujita scale. Wind Struct. 11 (4), 291–302.
Jischke, M.C., Light, B.D., 1983. Laboratory simulation of tornadic wind loads on a rectangular model structure. J. Wind Eng. Ind. Aerodyn. 13 (1–3), 371–382.
Kay, S.M., Marple, S.L., 1981. Spectrum analysis: a modern perspective. Proc. IEEE 69, 1380–1419.
Kikitsu, H., Sarkar, P.P., Haan, F.L., 2011. Experimental study on tornado-induced loads of low-rise buildings using a large tornado simulator. In: Proceedings of ICWE13.
Kuai, L., Haan, F.L., Gallus, W.A., Sarkar, P.P., 2008. CFD simulations of the flow field of a laboratory-simulated tornado for parameter sensitivity studies and comparison with field measurements. Wind Struct. 11 (2), 75–96.
Kumar, M., 2010. Minimum design loads for buildings and other structures (ASCE Standard 7-05).
Lilly, D.K., 1992. A proposed modification of the Germano subgrid-scale closure model. Phys. Fluids A4 (4), 633–635.
Liu, Z., Ishihara, T., 2015a. A study of tornado-induced mean aerodynamic forces on a gable-roofed building by the large eddy simulations. J. Wind Eng. Ind. Aerodyn. 146, 39–50.
Liu, Z., Ishihara, T., 2015b. Numerical study of turbulent flow fields and the similarity of tornado vortices using large-eddy simulations. J. Wind Eng. Ind. Aerodyn. 145, 42–60.
Matsui, M., Tamura, Y., 2009. Influence of swirl ratio and incident flow conditions on generation of tornado-like vortex. In: Proc. 5th European-African Conferences on Wind Engineering, Florence, Italy pp. 213-216.
Mishra, A.R., James, D.L., Letchford, C.W., 2008. Physical simulation of a single-celled tornado-like vortex, Part B: Wind loading on a cubical model. J. Wind Eng. Ind. Aerodyn. 96 (8), 1258–1273.
Monji, N., 1985. A laboratory investigation of the structure of multiple vortices. J. Meteorol. Soc. Japan 63, 703–712.
Nolan, D.S., Dahl, N.A., Bryan, G.H., Rotunno, R., 2017. Tornado vortex structure, intensity, and surface wind gusts in large-eddy simulations with full developed turbulence. J. Atmos. Sci. 74, 1573–1597.
Oka, S., Ishihara, T., 2009. Numerical study of aerodynamic characteristics of a square prism in a uniform flow. J. Wind Eng. Ind. Aerodyn. 97, 548–559.
Press, W.H., Teukolsky, S.A., Vetterling, W.T., et al., 2007. Numerical Recipes 3rd Edition: The Art of Scientific Computing. Cambridge University Press, pp. 681–685.
Rajasekharan, S.G., Matsui, M., Tamura, Y., 2013a. Characteristics of internal pressures and net local roof wind forces on a building exposed to a tornado-like vortex. J. Wind Eng. Ind. Aerodyn. 112, 52–57.
Rajasekharan, S.G., Matsui, M., Tamura, Y., 2013b. Ground roughness effects on internal pressure characteristics for buildings exposed to tornado-like flow. J. Wind Eng. Ind. Aerodyn. 122, 113–117.
Refan, M., Hangan, H., 2016. Characterization of tornado-like flow fields in a new model scale wind testing chamber. J. Wind Eng. Ind. Aerodyn. 151, 107–121.
Rotunno, R., Bryan, G.H., Nolan, D.S., et al., 2016. Axisymmetric tornado simulations at high Reynolds number. J. Atmos. Sci. 73 (10).
Rotz, J., Yeh, G., Bertwell, W., 1974. Tornado and extreme wind design criteria for nuclear power plants: Topical report. San Francisco, California.
Smagorinsky, J., 1963. General circulation experiments with the primitive equations. I. The basic experiment. Mon. Weather Rev. 91, 99–164.
Snow, J.T., 1982. A review of recent advances in tornado vortex dynamics. Rev. Geophys. 20 (4), 953–964.
Tari, P.H., Gurka, R., Hangan, H., 2010. Experimental investigation of tornado-like vortex dynamics with swirl ratio: the mean and turbulent flow fields. J. Wind Eng. Ind. Aerodyn. 98 (12), 936–944.
Wang, J., Cao, S., Pang, W., Cao, J., 2017. Experimental study on effects of ground roughness on flow characteristics of tornado-like vortices. Bound.-Layer Meteorol. 162 (2), 319–339.
Wang, J., Cao, S., Pang, W., Cao, J., Zhao, L., 2016. Wind-load characteristics of a cooling tower exposed to a translating tornado-like vortex. J. Wind Eng. Ind. Aerodyn. 158, 26–36.
Wurman, J., Alexander, C.R., 2005. The 30 may 1998 spencer, south dakota, storm. Part II: Comparison of observed damage and radar-derived winds in the tornadoes. Mon. Weather Rev. 133, 97–119.
Yang, Z., Sarkar, P., Hu, H., 2010. Visualization of flow structures around a gable-roofed building model in tornado-like winds. J. Vis. 13 (4), 285–288.
Yang, Z., Sarkar, P., Hu, H., 2011. An experimental study of a high-rise building model in tornado-like winds. J. Fluids Struct. 27 (4), 471–486.